L.Toni, E. F. Bellobuono, R. Valente, A. Romei, P. Gaetani, G. Persico, (2022) *Computational and experimental assessment of a MW-scale supercritical CO_2 compressor operating in multiple near-critical conditions*, J. Eng. Gas Turb. Power, Vol. 144(10), 101015 (10 pages), doi: 10.1115/1.4055364

COMPUTATIONAL AND EXPERIMENTAL ASSESSMENT OF A MW-SCALE SUPERCRITICAL CO_2 COMPRESSOR OPERATING IN MULTIPLE NEAR-CRITICAL CONDITIONS

Lorenzo Toni
Centrifugal Compressor and Expanders NPD
Baker Hughes, Nuovo Pignone,
Via F. Matteucci 2, Firenze 50127, Italy
lorenzo.toni@bakerhughes.com

Ernani Fulvio Bellobuono
Centrifugal Compressor and Expanders NPD
Baker Hughes, Nuovo Pignone,
Via F. Matteucci 2, Firenze 50127, Italy
ernani.bellobuono@bakerhughes.com

Roberto Valente
Centrifugal Compressor and Expanders NPD
Baker Hughes, Nuovo Pignone,
Via F. Matteucci 2, Firenze 50127, Italy
roberto.valente@bakerhughes.com

Alessandro Romei
Laboratory of Fluid Machines
Energy Department - Politecnico di Milano
Via Lambruschini 4, 20156 Milano, Italy
alessandro.romei@polimi.it

Paolo Gaetani
Laboratory of Fluid Machines
Energy Department - Politecnico di Milano
Via Lambruschini 4, 20156 Milano, Italy
paolo.gaetani@polimi.it

Giacomo Persico[1]
Laboratory of Fluid Machines
Energy Department - Politecnico di Milano
Via Lambruschini 4, 20156 Milano, Italy
giacomo.persico@polimi.it

ABSTRACT

The present work illustrates the results of a wide experimental campaign in the frame of the EU-funded project sCO2-Flex, focused on the investigation of a MW-scale sCO_2 compressor operating in plant-representative conditions. The experimental tests are carried out for four temperature levels between 304.15K and 309.15K at a fixed pressure of 79.79 bar, hence covering an extended

[1] Corresponding author

thermodynamic region close to the critical point. The experimental results are thoroughly discussed with the support of steady computational fluid-dynamics simulations, assuming homogeneous flows and thermodynamic equilibrium for the two-phase flow description. Changing the upstream total state, two peculiar variabilities in the compressor pressure ratio and in choking flow rate are experimentally and computationally observed. While the former is mainly related to the single-phase flow thermodynamics, the latter originates from the onset of two-phase flows. As the simulations predict the experimental choking with a maximum error of 3%, the corresponding two-phase speed of sound is analyzed to infer the underlying equilibria between phases. It is found that, for the tested conditions, two-phase flows quickly achieve thermodynamic equilibrium, and non-equilibrium or meta-stable effects arguably play a marginal role in the process.

Keywords: CO_2; supercritical fluid; centrifugal compressor; experiments; barotropic; HEM; speed of sound.

NOMENCLATURE

c	speed of sound
D_2	impeller diameter
h	enthalpy
k	compressibility coefficient
$\dot{m}$	mass flow rate
M	Mach number
M_{u2}	peripheral Mach number
P	pressure
s	specific entropy
T	temperatue
u_2	impeller outlet peripheral speed
v	velocity
y	vapor mass fraction

Subscripts

10	impeller inlet section
20	impeller outlet section

40 diffuser outlet section

c choking condition

d data

f flange section

HEM homogeneous equilibrium model

HFM homogeneous frozen model

l liquid

m mixture

sat saturation

T total

v vapor

Greek

α volume fraction

Δ difference

ρ density

ϕ flow coefficient

Π pressure ratio

Ψ head coefficient

1. INTRODUCTION

Using carbon dioxide as working fluid in both direct and inverse thermodynamic cycles is attractive for its low toxicity, thermal stability, and thermo-physical properties. Carbon dioxide in supercritical thermodynamic states (sCO_2 in the following) is potentially advantageous in power systems based on the closed Joule–Brayton cycles, due to the promise of high conversion efficiency and small component size [1, 2]. For these reasons, sCO_2 power systems are suited for operating in a flexible environment (such as in combination

with renewable sources and waste heat recovery) leveraging the expected good operational flexibility, which could realize potential benefits also for Floating Production Storage and Offloading applications.

The thermodynamic optimization of the sCO_2 power systems pushes towards recompressed/recuperative cycle configurations [3], which feature at least one compressor operating carbon dioxide close to its critical point and targeting a pressure ratio of the order of 3 [4]. Feasibility studies [5] recommend that, for system capacities within 300 MW, the compressor is of centrifugal type, thus the target pressure ratio is achievable using either a single-stage or a two-stage compressor.

Designing and operating high-speed turbomachinery working with sCO_2 in near-critical conditions entails aerodynamic and rotordynamic challenges whose proper mastering is instrumental for the success of the entire sCO_2 technology. Close to the critical point, the large gradients in density and specific heats make CO_2 thermodynamics deviate significantly from the ideal-gas law [6] and, due to the proximity to the saturation curve, phase-change phenomena can also take place within the bladed channels as a consequence of local flow accelerations [7]. The phase change can occur either as cavitation or condensation, depending on the entropy level of the CO_2 at the compressor intake, with important implications in terms of performance, rangeability, and mechanical integrity of the machine. Criteria for avoiding two-phase flows were proposed [8], which end up in severe limitations in the selection and design of the compressor, especially when considering appropriate dimensionless parameters for this class of turbomachinery.

Due to the low time-scale of the flow processes within compressor impellers, one potential advantage in the sCO_2 compressor operation might be the existence of metastable states, which result in a delay in the phase-change phenomena observed experimentally for condensing sCO_2 in nozzles [9]. However, approaching the critical point (where the metastable thermodynamic region becomes progressively thinner) the effect of meta-stable states is reduced and predictions based on the assumption of homogeneous equilibrium between phases exhibit an improved matching with experiments [10]. Similar findings were obtained when modeling experiments of flashing sCO_2 in nozzles [11].

In such an uncertain scenario, the availability of experiments is crucial to investigate the onset of phase transition and its implication on sCO_2 compressors. On the industrial ground, the phase transition might dramatically affect the aerodynamics, the performance, and the rangeability of the compressor [12]. From the scientific perspective, the modelling of two-phase compressible flows is still an open issue that involves computational challenges and demands a proper experimental assessment. Experiments on sCO_2 compressors are, in fact, available, but not always representative of the actual challenges of the sCO_2 technology. As a relevant example, experiments [13] and computations [14] were successfully performed on the compressor designed and operated at the Sandia National Laboratories (SNL); however, the available experimental data considered a small-scale prototype operated with a limited pressure rise, and no measurable effects of two-phase flow conditions were observed in the experimental compressor curves [15]. Relevant experimental studies on

exemplary sCO_2 compressors appear in [16], [17] and [18], in which sCO_2 compressor curves are reported, but again considering small-scale prototypes operated at relatively limited speed (and hence low peripheral Mach number, resulting in a limited aerodynamic loading and, ultimately, in pressure ratio below 1.5); in case of [17], authors purposely selected the thermodynamic state sufficiently far from saturation to avoid two-phase flows within the machine.

These considerations call for a crucial extension of the available database on sCO_2 compressors, considering experiments performed on real-scale turbomachinery operating in their actual thermodynamic conditions and experiencing realistic dimensionless parameters, e.g., in terms of peripheral Mach number. Very recently, the SWRI research team has contributed to filling this gap by publishing valuable experimental data on MW-scale compressors in realistic aero-thermodynamic conditions, focusing on rotordynamic [19, 20] and measurement [21] aspects. The present work, instead, aims at filling the gap on the aero-thermodynamic side of the problem, by presenting a unique set of experimental data and computational predictions performed on a MW-scale centrifugal compressor, designed in the frame of the EU-H2020 project sCO2-Flex, and featuring thermodynamic and operative conditions representative of those expected in the actual engineering application. sCO2-Flex proposes a novel cycle configuration oriented at improving the flexibility and efficiency of existing conventional power plants while minimizing water usage. The system includes an axial expander and two centrifugal compressors working in parallel, it is designed to provide 25 MWe at 100% load, and it has the flexibility to reduce load down to 20%; compared to a conventional water-steam plant, sCO2-Flex can reduce greenhouse gases emissions by 8%.

This paper is structured as follows. At first, the experimental and computational methodologies are discussed. Then, the experimental compressor curves are presented and compared to simulated trends, highlighting the role of non-ideal thermodynamics and phase change on the data. By virtue of the good agreement between experiments and simulations, important conclusions will be drawn on the physics of non-ideal two-phase flows of sCO2 and their proper modelling.

2. METHODS

In this paper we present a combined experimental and computational study of the prototype compressor under consideration. The challenges of the technology demanded the development of peculiar techniques for both approaches, which are described separately in the following.

2.1 Test rig and prototype compressor

The machine prototype is a 5.4 MW centrifugal compressor with variable-speed regulation (60%-105%), and nominal discharge pressure of 250 bar. A barrel-type casing was selected because of the high operating pressure. The rotor is composed by the shaft and

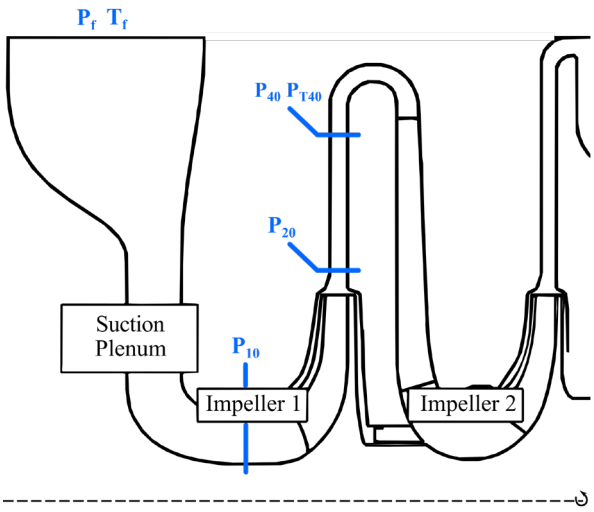

FIGURE 1: SCHEMATIC COMPRESSOR CROSS SECTION AND MEASUREMENT LOCATIONS.

two impellers. The first impeller has a dedicated design to cope with the peculiar thermodynamic features of sCO_2 in the proximity of the critical point, and it is the object of the present study. The second impeller belongs to the Baker Hughes centrifugal compressor stage database. The schematic cross-section of the machine is reported in Figure 1.

The experimental campaign was carried out on a test rig in the Baker Hughes facility in Florence, Italy. Tests comply with the ASME PTC-10 Type I, i.e., the compressor was operated under design conditions in terms of fluid composition, upstream total state, and operating conditions. The closed-loop test rig, schematized in Figure 2, includes: (i) a gas turbine to drive the compressor, (ii) a Venturi pipe downstream of the compressor to measure the mass flow rate (iii) a bypass loop to refine the control of the temperature at the compressor intake, (iv) a water cooler to set the temperature at the compressor intake, and (v) a regulation valve system.

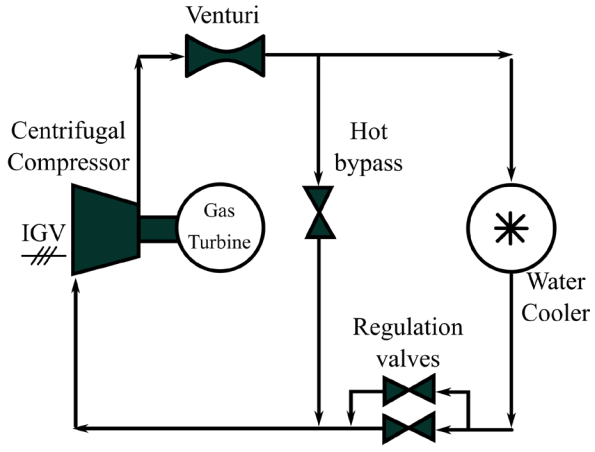

FIGURE 2: CENTRIFUGAL COMPRESSOR TEST RIG.

The instrumentation requires particular care due to large gradients in thermophysical properties close to the critical point, as pointed out by previous experimental experiences [21]. The instrumentation was placed in compliance with the ASME PTC-10 rule. Moreover, additional measurement locations are considered across the first-stage impeller to address a detailed experimental characterization of the component. Overall, the instrumentation consists of (i) four static pressure taps, one placed in the plenum, one upstream of the impeller, one downstream of the impeller after the channel pinch, and one towards the end of the vaneless diffuser, (ii) one resistance temperature detector (RTD) in the plenum, and (iii) one total pressure probe in correspondence of the last static pressure tap. The measurement locations and the measured quantities are sketched in Figure 1.

All instruments were purposely calibrated for the experimental campaign. The measurement uncertainty combines sensor accuracy and standard deviation of repeated test point acquisitions. The measurement uncertainties (or equivalent error bars) reported in the paper are always intended as expanded uncertainty, using a coverage factor of 2 (95% level of confidence assuming normal distribution).

The significant sensitivity of all fluid properties to temperature owing to the near-critical conditions imposes a severe limit on the uncertainty of temperature measurements to ensure the test-rig controllability and meaningful performance estimates. To this end, accurate temperature measurements were accomplished through an RTD class A+ calibrated with a primary source, returning an uncertainty of ± 0.04 K. This uncertainty value is almost one order of magnitude smaller than the uncertainty obtained with thermocouples in other experimental facilities (± 0.26 K [16], ± 0.25 K [21]). The static pressure measurements upstream of the impeller have a relative uncertainty of 0.1%, and it raises to 0.2% when the static pressure is measured downstream of the impeller. The relative uncertainty in the total pressure is 0.2%. The pressure uncertainty is comparably lower than the value declared in other experimental campaigns [16, 21]. The mass flow rate through the Venturi pipe is measured with a relative uncertainty of 0.8%. The relative uncertainty in rotational speed is below 0.01%, hence it is neglected in subsequent analyses.

2.2 Test matrix

The test matrix includes four supercritical total conditions, conveniently reported in the temperature - specific entropy state diagram in Figure 3. The selected upstream total states are representative of possible off-design conditions of the sCO2-flex project. Two upstream total states lie in the liquid-like domain ($s < s_c$), one state is in the neighborhood of the pseudo-critical line, i.e. the locus of the maximum isobaric heat capacity at a given temperature, and one state falls within the vapor-like region ($s > s_c$). The rotational speed is maintained constant at the value of 11405 rpm for all tests. Table 1 details the target thermodynamic states ($T_d,\ P_d$), the corresponding saturation pressure along the upstream isentrope (P_{sat}), and the peripheral Mach number ($M_{u2} = u_2/c_d$).

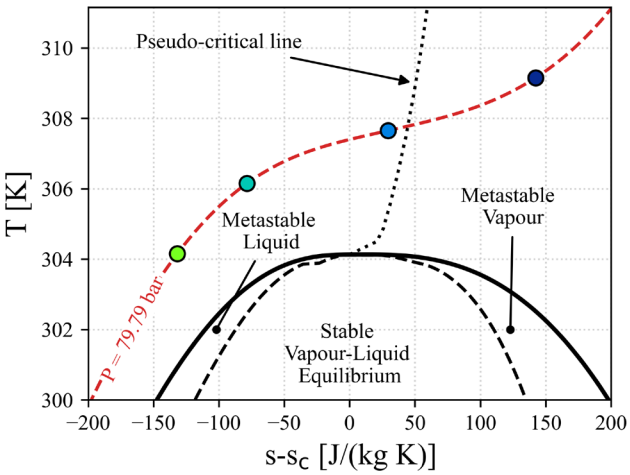

FIGURE 3: INTAKE THERMODYNAMIC STATES INCLUDED IN THE EXPERIMENTAL CAMPAIGN.

For each upstream total condition, the flow rate is varied to obtain samples of the compressor performance over the flow range. Each curve contains five test points, except for the curve at 306.15 K (representative of the design state of the sCO2-Flex project) that includes eight flow rates. The tests were performed to have an adequate representation of the right limit (choking) and to include at least one point at low flow rates. The tests at low flow rates were carried out away from surge to avoid compromising the test rig.

TABLE 1: TEST MATRIX AND OPERATING CONDITIONS

T_d [K]	P_d [bar]	P_{sat} [bar]	M_{u2}
304.15	79.79	68.56	0.56
306.15	79.79	72.20	0.68
307.65	79.79	73.76	0.85
309.15	79.79	71.10	0.80

As the compressor performance is expected to be sensitive to the upstream total state, particular care was dedicated to controlling the test rig in order to limit the variability across the flow range in thermodynamic conditions at the intake flange. Fine temperature regulation was obtained by means of the bypass valve (see again Figure 2), to divert, when needed, part of the flow upstream of the cooler. Figure 4 reports the deviation of pressure and temperature at the intake flange from the target values in Table 1 across the flow range expressed as flow coefficient normalized to its design value. The uncertainty propagation in total quantities and flow coefficient are comprehensively discussed in the next section. The maximum temperature deviation from the target value is 0.47 K $\pm$ 0.04 K, while the maximum deviation between two flow rates at the same target temperature is 0.62 K $\pm$0.08 K. Both maximum deviations are

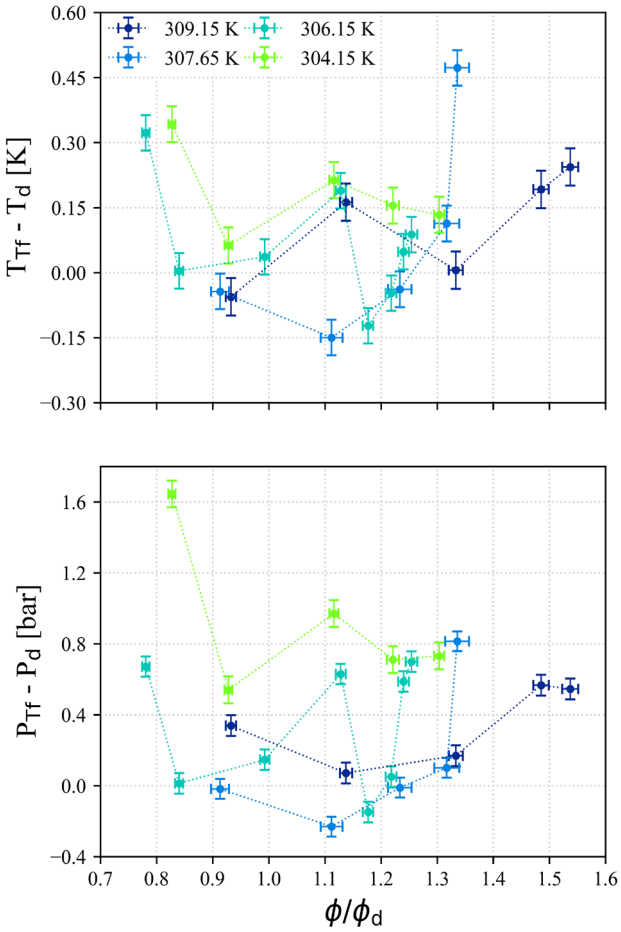

FIGURE 4: PRESSURE AND TEMPERATURE DIFFERENCES BETWEEN THE ACTUAL (P_D, T_D) AND FORESEEN (P_0, T_0) INLET CONDITIONS.

encountered for the upstream conditions close to the pseudocritical line, as the test-rig controllability is complicated by the largest gradients in fluid properties against temperature variations. The pressure deviation is within 1% of the target value for all tests, except for two points at the lowest target temperature. One point is slightly above 1%, while the last measured point deviates approximately 2% from the expected value. Despite these variations, both tests are included in the following analyses because they affect the target state that is farther from the critical point, thus the sensitivity from the upstream total state is expected to be less important.

2.3 Data processing and uncertainty quantification

The compressor performance is expressed in terms of either total-total pressure ratio Π or isentropic head coefficient Ψ across the flow range, which is conveniently reported in terms of flow coefficient ϕ. With reference to Figure 1, these quantities are calculated as:

$$\Pi = \frac{P_{T40}}{P_{T10}} \tag{1}$$

$$\Psi = \frac{H(P_{T40}, s_{10}) - h_{Tf}}{u_2^2} \tag{2}$$

$$\phi = \frac{\dot{m}}{\rho_{T10} u_2 D_2^2} \tag{3}$$

The flow coefficient is then normalized to the design value ϕ_d, which is the same among the four tested conditions. As discussed before, direct measurements of $\dot{m}, P_f, T_f, P_{10}, P_{20}, P_{40}$, and P_{T40} were obtained for each test. Additionally, the cross-sectional areas A_f and A_{10} are known.

The total state at the compressor flange is computed by first computing the total enthalpy as $h_{Tf} = h_f + 0.5\, v_f^2$, where $v_f = \dot{m}/(\rho_f A_f)$, and, then, by combining it with the specific entropy $s_f = S(P_f, T_f)$ to obtain total pressure and total temperature as $P_{Tf} = P(h_{Tf}, s_f)$ and $T_{Tf} = T(h_{Tf}, s_f)$, respectively. All thermodynamic functions are evaluated via the thermodynamic library RefProp, which features an equation of state explicit in the Helmholtz free energy for carbon dioxide [23].

Before computing the total state in section 10, the static state is computed iteratively by combining the static pressure measurement P_{10} with $h_{10} = h_{T10} - 0.5\, v_{10}^2$, where $h_{T10} = h_{Tf}$ as the inlet plenum can be assumed adiabatic. The iterative nature is hidden in the term $v_{10} = \dot{m}/(\rho_{10} A_{10})$, which implicitly includes the dependency on the static state in the density estimate, i.e., $\rho_{10} = \rho(P_{10}, h_{10})$. Therefore, the static state is obtained by iterating on the density and setting a maximum error of 1×10^{-6} kg/m^3 thereof. Once the static state is computed, the total state can be derived as a function of the total enthalpy h_{T10} and the specific entropy $s_{10} = s(P_{10}, h_{10})$.

The need for iterative algorithms to characterize the static and total state at the impeller inlet, as well as the implicit definition of thermophysical properties, prevent using analytical uncertainty propagation methods, e.g., based on Taylor series expansions. To overcome this issue, a Montecarlo method is used to propagate the uncertainty from direct measurements ($\dot{m}, P_f, T_f, P_{10}, P_{T40}$) to derived quantities of interest ($P_{Tf}, T_{Tf}, \phi, \Pi, \Psi$). The input uncertainties are assumed independent and distributed as normal distributions. 1×10^5 samples are randomly drawn from the input distributions and corresponding realizations of quantities of interest are computed as described above. The collection of realizations allows obtaining empirical probability density functions, from which the means and the corrected standard deviations are estimated for the target quantities. All output distributions can be approximated as normal distributions, since the maximum absolute values of skewness and excess of kurtosis are 0.05 and 0.14, respectively.

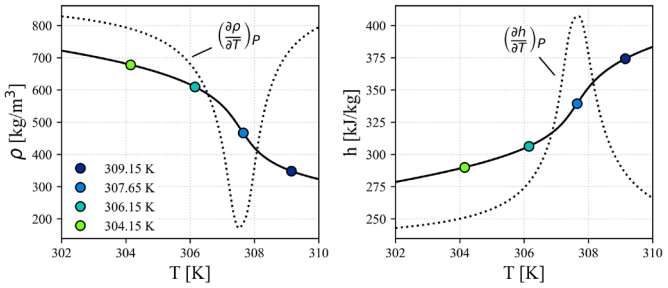

FIGURE 5: DENSITY AND SPECIFIC ENTHALPY EVOLUTION ACROSS THE TEMPERATURE FOR THE SELECTED ISOBAR AT $P = 79.79$ bar.

Table 2 reports the relative uncertainties for instrumentations and derived quantities at each temperature level, considering an arithmetic average over the test points. Due to the small kinetic head at the compressor flange, the corresponding uncertainty in total quantities is the same as the static measured values. Interestingly, the uncertainty in flow coefficient and isentropic head coefficient varies with the upstream total state, despite similar levels of uncertainty in primitive measurements. The highest uncertainty is found for the state at T=307.65 K. By looking at the state diagram in Figure 3, this point is relatively close to the pseudocritical line, whereby severe gradients in thermophysical properties exist, as also highlighted in Figure 5 for density and specific enthalpy. Such gradients amplify the uncertainty in the thermodynamic property estimates at the compressor inlet. As a result, the uncertainty in the flow coefficient almost doubles at T=307.65 K, and a significant increase is also noted for the isentropic head coefficient. Moving towards low temperature, the gradients attenuate, and the related uncertainties decrease. The dependency of uncertainty on the upstream total state is also observed by [21]. As a last comment, the uncertainty in the total-total pressure ratio is almost uniform over the considered test matrix. The only derived quantity that enters into Π is P_{T10}, which is computed from the direct measurement of P_{10}. The passage from static to total does involve the local flow thermodynamics, but this effect seems to be negligible. It follows that the corresponding uncertainty ($\sim 0.2\%$) is comparably smaller than the value reported in other studies [16].

TABLE 2: RELATIVE EXPANDED UNCERTAINTIES FOR THE MAIN QUANTITIES, AVERAGED OVER TESTS AT DIFFERENT FLOWS. ()

T [K]	304.15	306.15	307.65	309.15
INSTRUMENT UNCERTAINTY				
P_f	0.09%	0.07%	0.07%	0.07%
T_f	0.01%	0.01%	0.01%	0.01%
$\dot{m}$	0.77%	0.75%	0.79%	0.74%
P_{10}	0.07%	0.07%	0.06%	0.06%
P_{T40}	0.17%	0.18%	0.20%	0.21%
PROPAGATED UNCERTAINTY				
P_{Tf}	0.09%	0.07%	0.07%	0.07%
T_{Tf}	0.01%	0.01%	0.01%	0.01%
ϕ	0.77%	0.81%	1.69%	0.94%
Π	0.21%	0.21%	0.24%	0.23%
Ψ	0.39%	0.44%	1.29%	0.82%

2.4 Flow model and computational approach

The flow model applied in the Computational Fluid Dynamics (CFD) simulations performed in this study is based on the ANSYS-CFX finite-volume flow solver. The model makes use of high-order numerical schemes for both inviscid and viscous fluxes and introduces the effects of turbulence by resorting to the k-ω SST model [21], assuming fully turbulent flow. Considering the high Reynolds number as a consequence of the low kinematic viscosity of carbon dioxide in supercritical conditions, the assumption of hydraulically smooth surfaces is not appropriate and, hence, wall roughness and corresponding wall functions are specified.

A specific feature of the present model refers to the representation of the non-ideal thermodynamics of the fluid. This is crucial for the proper modelling of turbomachinery operating with sCO_2, whereby the proximity to the critical points originates a large departure from ideal-gas behavior. In particular, the thermodynamic description of the fluid is modelled here by resorting to the Span-Wagner equation of state [22]. However, the challenges of simulating the flow in technically-relevant sCO_2 compressors are also related to two-phase flows: the proximity of the inlet compressor state to saturation might trigger phase change phenomena that need to be introduced in the simulation model. To this end, in the present CFD model we resort to a barotropic fluid assumtion, in which the thermo-physical properties of the fluid (density and dynamic viscosity) are assumed only dependent on pressure; from a two-phase perspective, the barotropic model belongs to the class of homogeneous equilibrium models (HEM).

The barotropic relationships $\rho = \rho(P)$ and $\mu = \mu(P)$ are generated along the isentrope at the impeller inlet section (section 10 with reference to Figure 1) for each thermodynamic state. The barotropic model was first proposed for application to sCO_2 compressors by the same authors in [10], and it was validated against a complete HEM and experiments relevant for sCO_2 applications in [11].

The equations of motion were solved on a structured mesh composed of hexahedral elements. Meshes were generated applying AutoGridTM and included the main and splitter blade, with fillet radii, and the vaneless diffuser. A single blade passage was considered by exploiting periodic boundary conditions. As the aim is to investigate the internal flow aerodynamics, the inlet guide vanes, as well as the leaks in the seals and the related secondary flows, were not the object of the CFD simulation. After a preliminary grid-dependence analysis, a mesh composed by about 3 million elements was adopted. The resulting near-wall and core-flow resolutions were similar to those of the mesh used in previous numerical studies of the same authors [12].

Calculations were performed assigning the total state at section 10, taking an average value across the flow range for each upstream condition. The flow rate was imposed at the outflow, except close to choked-flow conditions, for which an average static pressure was assigned at the outlet. No-slip boundary conditions were imposed on the solid walls. As the flow domain is rotating with the impeller, a counter-rotating velocity was assigned at the endwalls of the vaneless diffuser.

3. RESULTS

This section presents experimental and computational data for the compressor operating at its nominal angular speed, for the intake thermodynamic states reported in Table 1. The experimentation and simulation of this class of machines introduces several technical and modeling challenges, which can be re-evaluated in light of the comparison discussed in Section 3.1. Section 3.2 proposes an interpretation of the most striking features emerging from the experiments, with the support of numerical simulations and theoretical considerations, to shed light on the aero-thermodynamic of sCO_2 compressors. The comparisons that will be presented in this chapter are intended to show the accuracy of pure CFD models of a centrifugal stage (impeller, diffuser, and return channel) without secondary elements like eye seal leakage, foot and disk friction in cavities whose effects are normally considered separately and added to the CFD outcome to get the complete stage performance prediction. Therefore, a slight over-estimate of pressure ratio from CFD if compared to test data is expected and well within the normal practice, whereas a very good agreement for curve shapes and operating range is demonstrated, see also [24].

3.1 Experimental and computational results

The maps of the sCO_2 compressor under study are reported in Figure 6, in terms of the total-total pressure ratio plotted against the normalized flow coefficient. Figure 6 reproduces, in solid lines, the experimental trends with their uncertainties and, in dashed lines, the corresponding trends predicted by numerical simulations. The selection of the pressure ratio as a primary quantity of interest is not only related to the reduced measurement uncertainty, but also to the relevance of this quantity in the perspective of the application of sCO_2

compressors in power systems. The achievement of the target pressure ratio in the expected range of operation, in terms of both flow coefficient and thermodynamic state, is indeed one of the cornerstones of the entire sCO_2 cycle technology.

The first aspect emerging from the measured data is the change in the pressure ratio provided by the compressor, once it is operated at different intake states. It has to be noted that, even though the value of the pressure ratio is not reported in the plot, the curves were

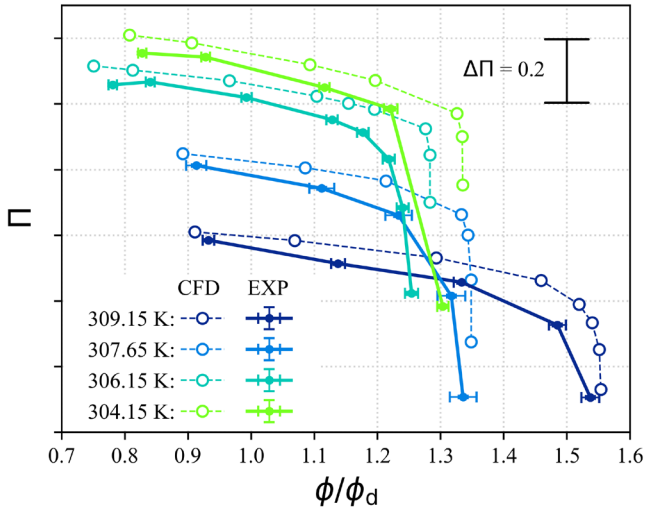

FIGURE 6: TOTAL-TOTAL PRESSURE RATIO MAP AS A FUNCTION OF FLOW COEFFICIENT FOR MULTIPLE INLET CONDITIONS.

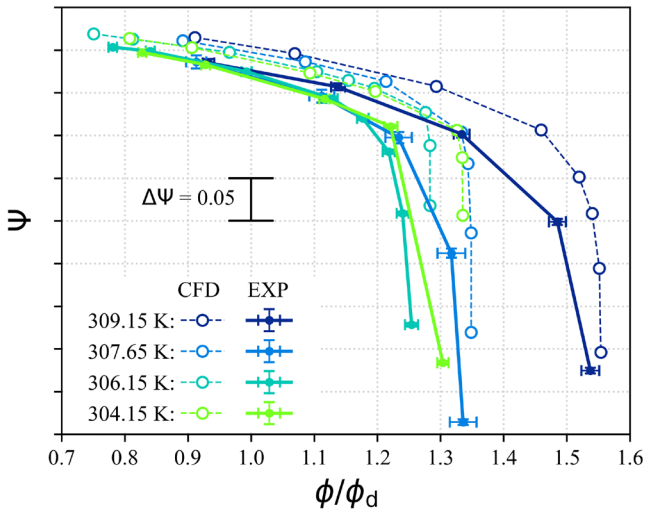

FIGURE 7: ISENTROPIC HEAD COEFFICIENT AS A FUNCTION OF FLOW COEFFICIENT FOR MULTIPLE INLET CONDITIONS.

not scaled, hence the graph reflects the actual difference among the curves. For comparison, Figure 7 reports the compressor curves reformulated in terms of isentropic head coefficient. Opposed to the pressure ratio, all isentropic head coefficient curves nearly collapse on a single one, at least in the region of low and design flow rate. This experimental evidence suggests that the enthalpy rise is weakly dependent on local flow thermodynamics but it is primarily related to the impeller aerodynamics via the Euler equation. Choking-related effects make the curves depart significantly at high flow rates.

Instead, as previously noted, the pressure ratio changes with the upstream total state. The physical explanation stems from the different fluid compressibility depending on the local thermodynamic state. Given the same enthalpy content, the pressure varies in accordance with the inherent fluid compressibility modulated by the Mach number, as clearly visible from the following expression:

$$\Psi \approx \frac{1}{M_{u2}^2} \frac{1}{k-1} \left(\Pi^{\frac{k-1}{k}} - 1 \right), \tag{4}$$

where

$$k = \frac{\rho}{P} \left(\frac{\partial P}{\partial \rho} \right)_s \tag{5}$$

is a measure of fluid compressibility [6, 25]. k tends to infinity under the incompressible fluid approximation, while it equates to the ratio among specific heats under the ideal-gas hypothesis. Equation (4) holds in an approximate manner because k is taken as constant (averaged) instead of varying along the compression, but this approximation does not alter the general trend [25].

Equation 4 states that the pressure ratio increases as k increases for the same head coefficient and peripheral Mach number. The present experiments confirm that, in a context of substantial equivalence of Ψ, the pressure ratio increases as the reduction of intake total temperature raises k, which passes from 1.6 at 309.15 K to 6.3 at 304.15 K. Because of the temperature change, the peripheral Mach number also reduces from 307.65 K to 304.15 K, partially counterbalancing the effect of k. Nevertheless, the change due to the intake thermodynamic state amounts to about 0.5 in terms of $\Delta\Pi$ in the region of the curve around the design flow rate, resulting quantitatively very significant.

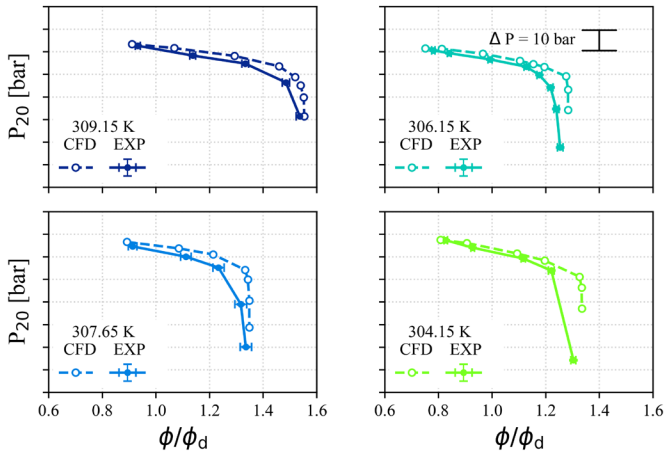

FIGURE 8: STATIC PRESSURE CURVES FROM EXPERIMENTS AND SIMULATIONS AT THE IMPELLER EXIT STATION FOR MULTIPLE INLET CONDITIONS.

The numerical simulations slightly overestimate the total pressure ratio (for the reasons recalled at the beginning of Section 3), but they correctly reproduce the experimental trends across the flow range and their dependence on the intake thermodynamic state. To enrich the database of experimental data here reported, the curves of static pressure at the exit of the impeller (section 20) and towards the outlet of the vaneless diffuser (section 40) are reported alongside their computational counterparts in Figures 8 and 9, respectively. The computational curves follow the experimental trends in both traverse measurements across the whole flow range. As a final note on the curve assessment, by comparing the plots reported in Figure 6 and 9 one can further infer that the predicted pressure curves match

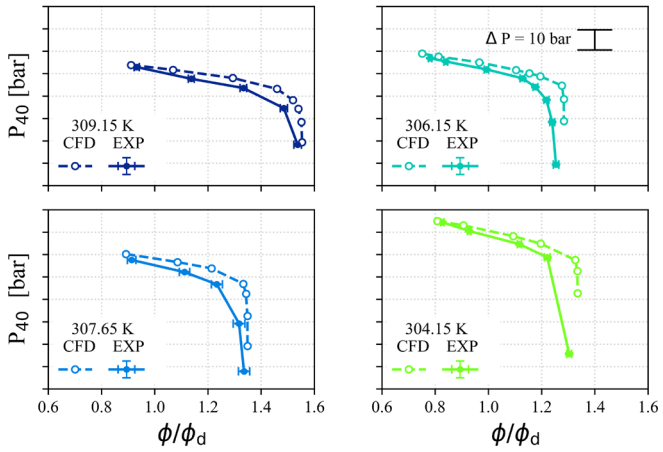

FIGURE 9: STATIC PRESSURE CURVES FROM EXPERIMENTS AND SIMULATIONS AT THE DIFFUSER EXIT STATION FOR MULTIPLE INLET CONDITIONS.

the experimental ones with a similar level of accuracy for the static and total pressure, thus suggesting that also the dynamic pressure is well predicted.

An interesting feature of the compressor map is the large variability among the curves in the region close to the choking conditions, which clearly appears for all the states analyzed. As a first consideration, the choking limit changes considerably among the different intake conditions, and differently from what one might expect considering the difference in peripheral Mach number among the curves. As a further consideration, the performance drop connected to choking occurs in a limited flow range for the two lowest temperature values, while it is progressively distributed on a larger flow range as the temperature increases. Due to this abrupt drop in pressure ratio (or static pressure values) large pressure differences locally appear between experiments and simulations, which could be partially due to a lack of resolution in the tested conditions in the proximity of the choking limit. This is also suggested by analyzing the numerical and experimental curves obtained for the highest intake temperature, which exhibit a smoother performance decay, and the comparison between the experiment and simulation improves accordingly. Despite these differences in the local pressure values, the choking flow rate is matched within 3% by the computational model, as highlighted in Table 3.

TABLE 3: COMPARISON OF CHOKED FLOW RATE BETWEEN SIMULATIONS AND EXPERIMENTS.

	ϕ_c/ϕ_d	
T [K]	**CFD**	**EXP**
304.15	1.335	1.304 ± 0.005
306.15	1.283	1.254 ± 0.005
307.65	1.348	1.336 ± 0.021
309.15	1.554	1.537 ± 0.014

As found for the change in pressure ratio, also the onset of choking appears governed primarily by the thermodynamics of the fluids, with a lower choking flow rate found for the lower temperature values. An exception is found for the second case (306.15 K), which exhibits the lowest choking limit despite not being operated at the lowest temperature. However, the temperature level is not explanatory, by itself, of the process occurring within the compressor, and a physical interpretation is required to properly comprehend the underlying physics originating from the choking phenomena here observed.

As commented previously, sCO_2 compressors operating close to the critical point are prone to experience fluid phase transition within the impeller channels. With reference to the four cases here considered, for the two lowest temperatures the phase change occurs as cavitation, while it occurs as condensation for the highest temperature; the third case is close to the pseudo-critical line, and the phase change occurs near the critical point. As well known [26], the onset of phase change is connected to an abrupt reduction of speed of

sound and, consequently, to an increase of Mach number. This latter can lead to the onset of choking, as already conceptualized by the same [12] and other [27, 28] authors in previous computational studies. A key feature of two-phase flows is, therefore, the estimate of the speed of sound, which stems from the physical model used to reproduce the two-phase flow, and changes according to the degree of equilibrium between the co-existing phases. The present experimental and numerical analyses allow shedding light on the phenomena occurring in such flows, thus contributing to extract relevant information for the modeling of two-phase flows in sCO_2 compressors. This analysis is proposed in Section 3.2.

3.2 Speed of sound analysis and effects on choking

One critical parameter to estimate when dealing with compressible multi-phase flows is the speed of sound of the mixture. The speed of sound is not an extensive quantity; hence it cannot be evaluated by averaging the speed of sound of individual phases over mass fractions. A multiplicity of approaches have been proposed in the literature for evaluation of the speed of sound, the most important of those are described in Brennen's book [26]. In the present context, we focus on a simplified representation of the two-phase flow, namely the so-called two-fluid model. In such a model, the two-phase flow is considered composed of a primary phase and a secondary phase, which is assumed to be dispersed into the former. The two phases are considered mixed to generate a continuous fluid, whose thermo-physical properties are evaluated by resorting to proper mass and volume averages of those of the individual phases. Such assumptions are recovered in the physical model of the present CFD simulations.

On top of the two-fluid formulation, the CFD model introduces an additional hypothesis in the two-phase flow physics, assuming homogeneous flow (same velocities between phases) and thermodynamic equilibrium. Under this framework, the speed of sound can be evaluated according to the standard definition by using the mixture density ρ_m:

$$c_{HEM}^2 = \left(\frac{\partial P}{\partial \rho_m}\right)_s \tag{6}$$

A few authors adopted the HEM framework for the simulation of sCO_2 compressors [14, 29], although expression (6) did not explicitly appear in their paper. The problem associated with the reduction in speed of sound was not discussed in these past works because they mainly focused on the CFD model validation against SNL experimental data [13]. As also stated in the introduction, the SNL compressor was tested in operating conditions less severe with respect to the present ones (e.g., smaller peripheral Mach number), not representative of the technical applications. Such conditions hinder the premature choking discussed in this work.

In general, the two-fluid model does not strictly require thermodynamic equilibrium. If the two phases are assumed adiabatic, according to the so-called homogeneous frozen model (HFM), an alternative formulation for the estimate of the speed of sound is available [30]. The mathematical formulation involves the harmonic average between the volumetric-weighted bulk moduli of the two phases as:

$$\frac{1}{\rho_m c_{HFM}^2} = \frac{\alpha_l}{\rho_l c_l^2} + \frac{\alpha_v}{\rho_v c_v^2} \qquad (7)$$

where α is the volume fraction, and subscripts l and v refer to the liquid and vapor phase, respectively. Although expression (7) is most representative of non-reactive two-phase flows of different fluids (e.g., bubbles of air dispersed in water), a number of studies related to sCO_2 compressors considered this definition [28, 31].

Figure 10 reports the trend of the speed of sound along isentropic expansions for the tested intake conditions, according to equation 6 (left) and equation 7 (right). After a progressive reduction of the single-phase speed of sound approaching the saturation, the HEM predicts an abrupt drop in speed of sound (discontinuous at saturation), while the HFM predicts continuous non-monotonic trends, which can even exceed the corresponding single-phase value. It is concluded that the HEM and the HFM represent the two extremes between complete equilibrium and non-equilibrium conditions. Any intermediate model that relaxes one or more equilibrium hypotheses features a speed of sound included in-between the two aforementioned models [32]. Therefore, the consistent CFD prediction of the experimental choking can be exploited to identify the most suitable model for sCO_2 compressor applications.

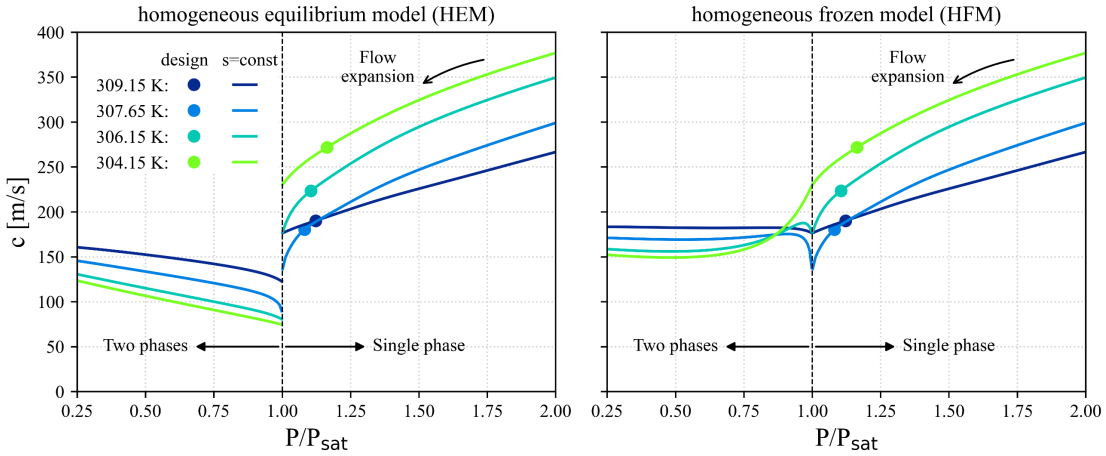

FIGURE 10: SPEED OF SOUND OF THE TWO-PHASE MIXTURE ASSUMING THERMODYNAMIC EQUILIBRIUM (LEFT) OR NEGLECTING HEAT AND MASS TRANSFER BETWEEN PHASES (RIGHT).

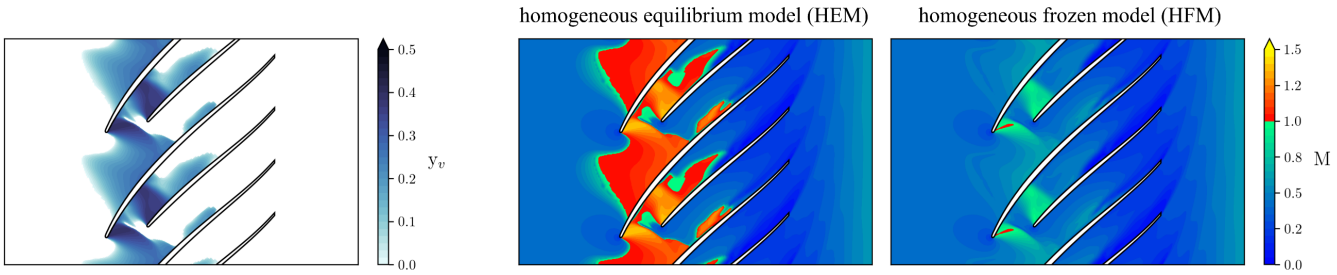

FIGURE 11: BLADE-TO-BLADE FLOW CONFIGURATION AT MIDSPAN CLOSE TO CHOKING (306.15 K): LEFT: VAPOUR MASS FRACTION; RIGHT: MACH NUMBER – COMPARISON OF TWO SPEED OF SOUND FORMULATIONS.

To this end, a post-processing of the cavitating flow is considered in Figure 11 for the choked-flow condition at the upstream temperature of 306.15 K. By focusing on the impeller midspan section, the mass fraction of vapor covers the whole intake region, including the throat. The appearance of the secondary phase originates from the local acceleration of the flow, as a combination of blade blockage, suction on the blade surface, and local acceleration at the leading edge due to the off-design (negative) incidence. As shown in Figure 11 (middle frame), if the flow velocity is processed in combination with the HEM speed of sound, the abrupt drop in speed of sound due to the phase change results in an abrupt rise in Mach number, which exceeds unity and leads to the choked-flow condition.

Assuming now to freeze the vapor fraction and that the mixture velocity is weakly affected by the local two-phase interaction, the Mach number can be evaluated in accordance with the HFM speed of sound. For this case, the flow remains largely subsonic, reporting a Mach number of 0.8 at the throat. It follows that, if it were the case, choking would have not occurred in this condition. This analysis, coupled with the experimental evidence of choking, supports that two-phase flows onsetting close to the critical point quickly achieve the thermodynamic equilibrium, and non-equilibrium or meta-stable effects arguably play a marginal role. Since a high level of agreement was systematically found between experiments and simulations in terms of choking flow rate, the aforementioned conclusion can be extended to all the states of interest of this study, which cover a wide range of applications for sCO_2 compressors.

4. CONCLUSION

This paper has presented a combined experimental and computational study of the aero-thermodynamics of a MW-scale compressor operating with supercritical carbon dioxide, operated for four intake thermodynamic states close to the critical point. The experiments had to face several measurement challenges connected to the nature of the fluid and the specific conditions of operation of the compressor. As all the four states are in a thermodynamic region characterized by a significant sensitivity of thermophysical fluid properties to temperature, particular attention was paid to control the test rig, managing to limit the variability in the intake total

temperature to around 0.5 K among the different tests. For the same reason, all the instruments involved in the tests were purposely calibrated, thus limiting their uncertainty (the one on temperature measurement in particular). Finally, to quantify the uncertainty levels of the derived performance data, a rigorous uncertainty propagation procedure was developed and applied by resorting to the Montecarlo method. The numerical simulations of the compressor under study had to consider both the non-ideality of the fluid and the potential onset of two-phase flow within the impeller channels (since all the states of interest are close to saturation). To this end, the thermodynamics of the fluid within the CFD model was introduced by resorting to a barotropic model, which, in case two-phase flows establish, assumes homogeneous equilibrium between the two phases. The experimental and computational maps of the compressor have been systematically compared, showing a slight over-estimate of pressure ratio from CFD (justified by the simplifications in the geometrical representation of the machine with respect to the test-rig configuration), whereas a very good agreement for curve shapes and operating range has been found for all the conditions. The curves of the compressor evidence a large dependence of the pressure ratio on the compressibility level of the fluid, which changes significantly among the four intake states considered; the isentropic head coefficient is instead weakly dependent on the intake state, except in the choking region where large variations appear. The calculations reproduce appropriately the dependence of the compressor operation on the compressibility of the fluid and predict the choking limit in flow rate within 3% of the experimental datum. Simulations clearly show that, for all the tested conditions, choking is triggered by the onset of two-phase flows within the impeller, as a consequence of the drop of the speed of sound of the mixture. A comparison among different models available to estimate the speed of sound of two-phase mixtures suggests that non-equilibrium or meta-stable effects play a marginal role in this class of two-phase flows.

Considering the capability of the present CFD simulations in predicting the choking limit for all the conditions of the present experiments, which cover a wide range of sCO_2 applications, we conclude that: (i) the choking observed in the experiments is connected to the phase change and the subsequent drop in speed of sound; (ii) the homogeneous equilibrium model applied in the CFD simulations is accurate for the prediction of choking driven by the onset of two-phase flow in sCO_2 compressors. In light of these findings, a HEM-based CFD modeling of two-phase flows can be reliably applied for the design and analysis of sCO_2 compressors.

5. ACKNOWLEDGMENT

This work was supported by the sCO2-Flex project, funded from the European Union's Horizon 2020 research and innovation programme under grant agreement N° 764690.

The authors would like to express their gratitude to Baker Hughes for providing the permission to proceed with publication and to Massimo Camatti for supporting this activity.

Thanks are due to Silvia Evangelisti, Giuseppe Nasca, and Stefano Vanghi from Baker Hughes' Turbomachinery Testing Laboratory (TTL).

REFERENCES

[1] Angelino, G., *Carbon dioxide condensation cycles for power production*, ASME Paper No. 68-GT-23, J. Eng. Power 90, 1968.

[2] Lee, J. I. Lee, H. J. Yoon, and J. E. Cha, *Supercritical Carbon Dioxide Turbomachinery Design for Water-Cooled Small Modular Reactor Application*, Nucl. Eng. Des., vol. 270, pp. 76-89, 2014.

[3] Alfani, D., Binotti, M., Macchi, E., Silva, P., Astolfi, M., *sCO2 power plants for waste heat recovery: Design optimization and part-load operation strategies*, Applied Thermal Engineering, Vol. 195, 117013.

[4] A. Romei, P. Gaetani, A. Giostri and G. Persico, *The role of turbomachinery perfomance in the optimization of supercritical carbon dioxide power systems*, Journal of Turbomachinery, vol. 142, no. 7, p. 071001, 2020.

[5] K. Brun, P. Friedman and R. Dennis, *Fundamentals and Applications of Supercritical Carbon Dioxide (sCO2) Based Power Cycles*, Woodhead Publishing, 2017.

[6] N. D. Baldadjiev, C. Lettieri and Z. S. Spakovszky, *An investigation of real gas effects in supercritical CO2 centrifugal compressors*, Journal of Turbomachinery, vol. 137, no. 9, p. 091003, 2015.

[7] C. Lettieri, N.D. Baltadjiev, M. Casey, Z.S. Spakovszky, *Low-flow-coefficient centrifugal compressor design for supercritical CO2*, J. Turbomach., Vol. 136, 081008, 2014.

[8] T. C. Allison and A. McClung, *Limiting Inlet Conditions for Phase Change Avoidance in Supercritical CO2 Compressors*, in Proceedings of ASME Turbo Expo 2019, Phoenix, Arizona, USA , 2019

[9] C. Lettier, D. Paxson, Z. Spakovszky and P. Bryanston-Cross, *Characterization of nonequilibrium condensation of supercritical carbon dioxide in a de laval nozzle*, Journal of Engineering for Gas Turbines and Power, vol. 140, no. 4, p. 041701, 2017.

[10] A. Romei and G. Persico, *Computational fluid-dynamic modeling of two-phase compressible flows of carbon dioxide in supercritical conditions*, Applied Thermal Engineering., Vol. 190, 2021

[11] M. Nakagawa, M.S. Berana, A. Kishine, *Supersonic two-phase flow of CO2 through converging–diverging nozzles for the ejector refrigeration cycle*, Int. J. Refrig. 32, 1195–1202, 2009.

[12] G. Persico, P. Gaetani, A. Romei, L. Toni, E. Bellobuono, R. Valente, *Implications of phase change on the aerodynamics of centrifugal compressors for supercritical carbon dioxide applications*, J. Eng. Gas Turbines Power 143 (4), 041007, 2021.

[13] S. Wright, R. Radel, M. Vernon, G. Rochau and P. Pickard, *Operation and Analysis of a Supercritical CO2 Brayton Cycle*, SANDIA REPORT, SAND2010-0171, Albuquerque, New Mexico, 2010.

[14]. R. Pecnik, E. Rinaldi and P. Colonna, *Computational fluid dynamics of a radial compressor operating with supercritical CO2*, Journal of Engineering for Gas Turbines and Power, vol. 134, no. 12, p. 122301, 2012.

[15] Noall, J. S., and Pasch, J. J., 2014, *Achievable Efficiency and Stability of Supercritical CO2 Compression Systems Main Compressor Design Discussion*, The 4th International Symposium—Supercritical CO2 Power Cycles, Pittsburgh, PA, Sept. 2014, pp. 1–10.

[16] Hacks, A., Vojacek, A., Dohmen, H., and Brillert, D., *Experimental investigation of the sCO2-HeRo compressor*, 2nd European sCO2 Conference, p. 50-59, 2018.

[17] S. K. Cho, S. Son, J. Lee, S-W. Lee, Y. Jeong, B. S. Oh, J. I. Lee, *Optimum loss models for performance prediction of supercritical CO2 centrifugal compressor*, Applied Thermal Engineering, Vol. 184, 2021, 116255.

[18] Clementoni, E., *Comparison of compressor performance map predictions to test data for a supercritical carbon dioxide Brayton power system*, Proceedings of the ASME Turbo Expo, GT2021-58763, June 7-11, 2021, Virtual Conference.

[19] Cich, S., Moore, J., Kulhanek, C., Mortzheim, J., 2020, *Development and Testing of a Supercritical CO2 Compressor Operating Near the Dome*, Turbomachinery and Pump Symposia, Texas A&M University, Houston, TX, September 15-17, 2020.

[20] Cich, S., Moore, J., Kulhanek, C., Towler, M., Mortzheim, J., 2021, *Mechanical Design and Testing of a 2.5 MW SCO2 Compressor Loop*, Proceedings of the ASME Turbo Expo, GT2021-04155, June 7-11, 2021, Virtual Conference.

[21] Mortzheim, J., Hofer, D., Piebe, S., McClung, A., Jeffrey Moore, J., Cich Stefan, *Challenges with Measuring Supercritical CO2 Compressor Performance When Approaching the Liquid-Vapor Dome*, Proceedings of the ASME Turbo Expo, GT2021-59527, June 7-11, 2021, Virtual Conference.

[22] F. R. Menter, *Two-Equation Eddy-Viscosity Turbulence Models for Engineering Applications*, AIAA Journal, vol. 32, no. 8, pp. 1598-1605, 1994.

[23] R. Span and W. Wagner, *A New Equation of State for Carbon Dioxide Covering the Fluid Region from the Triple-Point Temperature to 1100 K at Pressures up to 800 MPa,* Journal of Physical and Chemical Reference Data, vol. 25, no. 6, pp. 1509-1596 , 1996.

[24] E. Guidotti, L. Toni, D.T. Rubino, L. Tapinassi, G. Naldi, V.V.N.K.S. Koyyalamudi, S. Prasad, *Influence of Cavity Flows Modeling on Centrifugal Compressor Stages Performance Prediction Across Different Flow Coefficient Impellers*, Proceedings of the ASME Turbo Expo, 2014, GT2014 - 25830

[25] Pham, H.S., Alpy, N., Ferrasse, J.H., Boutin, O., Tothill, M., Quenaut, J., Gastaldi, O., Cadiou, T., and Saez, M., *An approach for establishing the performance maps of the sc-CO 2 compressor: Development and qualification by means of CFD simulations,* International Journal of Heat and Fluid Flow, vol 61, pp 379-394, 2016.

[26] C.E. Brennen, *Homogeneous flows*, in: Fundamentals of Multiphase Flow, Cambridge University Press, 2005, pp. 176–198.

[27] F. Moraga, D. Hofer, S. Saxena, R. Mallina, *Numerical Approach for Real Gas Simulations: Part I – Tabular fluid properties for real gas analysis*, Proceedings of the ASME Turbo Expo 2017, no. GT2017-63148, 2017.

[28] S. Saxena, R. Mallina, F. Moraga, D. Hofer, *Numerical Approach for Real Gas Simulations: Part II – Flow Simulation for Supercritical CO2 Centrifugal Compressor*, Proceedings of the ASME Turbo Expo 2017, no. GT2017-63149, 2017.

[29] R.E. Karaefe, P. Post, M. Sembritzky, A. Schramm, F. di Mare, M. Kunick, U. Gampe, *Numerical Investigation of a Centrifugal Compressor for Supercritical CO2 Cycles*, Proceedings of the ASME Turbo Expo 2020, no. GT2020-15194, 2020.

[30] A.B. Wood, *A Textbook of Sound: Being an Account of the Physics of Vibrations with Special Reference to Recent Theoretical and Technical Developments*, The Macmillan company, New York, 1941.

[31] M. Anderson, *Compressor Map Corrections for Highly Non-Linear Fluid Properties*, in Proceedings of the ASME Turbo Expo 2021, no. GT2021-60275, 2021

[32] T. Flatten, H. Lund, *Relaxation two-phase flow models and the subcharacteristic condition*, Math. Models Methods Appl. Sci. 21 (12) (2011) 2379–2407.